The Astrophysical Journal, 927:225 (11pp), 2022 March 10 https://doi.org/10.3847/1538-4357/ac5326

Unveiling the Origin of the Fermi Bubbles with MeV Photon Telescopes

Michela Negro[1,2,3], Henrike Fleischhack[2,3,4], Andreas Zoglauer[5], Seth Digel[6], and Marco Ajello[7]
[1] University of Maryland, Baltimore County, Baltimore, MD 21250, USA; mnegro1@umbc.edu
[2] NASA Goddard Space Flight Center, Greenbelt, MD 20771, USA
[3] Center for Research and Exploration in Space Science and Technology, NASA/GSFC, Greenbelt, MD 20771, USA
[4] Catholic University of America, 620 Michigan Avenue NE, Washington, DC 20064, USA
[5] Space Sciences Laboratory, University of California at Berkeley, 7 Gauss Way, Berkeley, CA 94720, USA
[6] KIPAC/SLAC, 2575 Sand Hill Road, Menlo Park, CA 94025, USA
[7] Department of Physics and Astronomy, Clemson University, Clemson, SC 29634, USA
Received 2021 November 18; revised 2022 February 3; accepted 2022 February 7; published 2022 March 21

Abstract

The Fermi Bubbles (FBs) are a pair of large-scale ellipsoidal structures extending above and below the Galactic plane almost symmetrically aligned with the Galactic center. After more than 10 yr since their discovery, their nature and origin remain unclear. Unveiling the primary emission mechanisms, whether hadronic or leptonic, is considered to be the main tool to shed light on the topic. We explore the potential key role of MeV observations of the FB, and we provide a recipe to determine the sensitivity of Compton and Compton-pair telescopes to the extended emission of the FB. We illustrate the capabilities of the Imaging Compton Telescope COMPTEL, the newly selected NASA MeV mission Compton Spectrometer and Imager, as well as the expectations for a potential future Compton-pair telescope such as the All-sky Medium Energy Gamma-ray Observatory eXplorer.

Unified Astronomy Thesaurus concepts: Gamma-ray telescopes (634); Stellar wind bubbles (1635); Gamma-rays (637)

1. Introduction

More than 10 yr have passed since the Fermi Bubbles (FBs) were discovered (Dobler et al. 2010; Su et al. 2010). These Galactic-scale structures, extending, almost symmetrically, above and below the Galactic plane, have been observed, analyzed, and physically interpreted in numerous and diverse studies, and yet their nature, their origin, and their emission mechanisms are still under investigation. Detections of the emission of the FB peaks in the GeV gamma-ray band, the domain of the Fermi Large Area Telescope (LAT) since 2008 (Atwood et al. 2009). Ackermann et al. (2014) have provided detailed measurement and analysis of the FB between 100 MeV and 500 GeV beyond 10° from the Galactic plane. Analyses have revealed that the intensity spectrum is almost spatially uniform within the sharp edges of the bubbles (Dobler et al. 2010; Dobler 2012; Planck Collaboration 2013; Ackermann et al. 2014), and it is well represented by a power law with a hard photon spectral index (∼−2) and an exponential cutoff at high energies (∼110 GeV). The FB interestingly overlaps (at $|b| < 35°$) with another long-known elephant[8] in the sky: the so-called microwave haze, observed by WMAP[9] (Su & Finkbeiner 2012; Rubtsov & Zhezher 2018). The similarity of their shapes is impressive, making the association between the two giants very straightforward.

At latitudes within 10° from the Galactic plane, Herold & Malyshev (2019) found GeV intensities greater than those at high latitudes with a spectrum well described by a single power law between 10 GeV and 1 TeV, and, interestingly, the axis perpendicular to the plane of the Milky Way was found to be shifted to the west of the Galactic center (GC), which undermines the generally accepted hypothesis that the origin of the FB is associated with the GC.

The observation of the FB at TeV energies is the territory of ground-based gamma-ray observatories. So far, no significant emission has been observed in that energy range. The High Altitude Water Cherenkov (HAWC) observatory[10] derived stringent upper limits on the very-high-energy gamma-ray emission from the northern FB (outside the Galactic plane) above 1.2 TeV (Abeysekara et al. 2017). These measurements provide further support for an exponential cutoff in the energy spectrum and rule out the presence of a second component at very high energies.

There have been some indications that the spectrum of the FB near the GC may be harder, even presenting a feature peaking between 1 and 4 GeV (Hooper & Slatyer 2013), and could extend to higher energies compared to the rest of the bubbles (Ackermann et al. 2017; Herold & Malyshev 2019). However, such results suffer from large systematic uncertainties due to the complicated modeling of the interstellar diffuse and discrete source gamma-ray emission of the GC region, which may result in contamination by nonmodeled components (e.g., unresolved pulsar wind nebulae; Vecchiotti et al. 2021). A recent study by the H.E.S.S. Collaboration[11] found no significant emission from the low-latitude part of the bubbles, constraining the exponential cutoff in the energy spectrum to be between 700 GeV and 1.7 TeV (Moulin et al. 2021).

The eROSITA telescope (Merloni et al. 2012) recently reported an X-ray counterpart, the eROSITA bubbles (eRBs; Predehl et al. 2020). The eRBs have a morphology different from that of the FB: they are larger, more spherical, and show

[8] Elephants in the gamma-ray sky: https://cerncourier.com/a/elephants-in-the-gamma-ray-sky/.
[9] https://map.gsfc.nasa.gov
[10] https://www.hawc-observatory.org/
[11] https://www.mpi-hd.mpg.de/hfm/HESS/

brighter edges with respect to the inner regions. It has been argued that the eRBs and FBs must be related due to their positional concentricity. The observed average X-ray surface brightness reported in Predehl et al. (2020) is almost two orders of magnitude above the FB gamma-ray intensity,[12] which roughly corresponds to $(1.5–3) \times 10^4$ eV cm^{-2} s^{-1} sr^{-1}. This mismatch might be indicative of different energy sources behind the two pairs of bubbles. More studies are needed to understand the connection, if any, between the FBs and the eRBs.

Where and how did the FB originate? Although measuring the distance of the FB along the line of sight is not straightforward, it is appealing to assume their coincidence with the GC, given their shape projected on the sphere. In this scenario, previous publications distinguish between an origin due to nuclear star formation activity near the GC and past jet-like activity associated with the supermassive black hole in the center of the Milky Way. In both of these scenarios, cosmic rays (CRs) are produced and accelerated close to the Galactic plane and then transported farther out by strong winds (Yang & Ruszkowski 2017). Once the FB are inflated, two possible emission mechanisms can contribute to the observed GeV emission: hadronic and leptonic processes, depending on the nature of the main species of particles involved.

Hadronic processes involve CR protons (CRp) interacting with thermal nuclei in the vicinity of the GC, producing short-lived mesons such as neutral and charged pions. The majority of the observed GeV gamma-ray emission would be associated with π^0 decay. However, other decay products of hadronic mechanisms comprise a population of secondary leptons, including electrons and positrons (CRe), which produce additional gamma rays via inverse-Compton (IC) scattering, and high-energy neutrinos. The latter are indeed expected to contribute to the astrophysical neutrino flux detected by the high-energy neutrino observatories, such as IceCube[13] and ANTARES.[14] Recent works have derived upper limits on the neutrino flux from the FB considering both the LAT observation and the HAWC upper limits (Adrián-Martínez et al. 2014; Fang et al. 2017; Razzaque & Yang 2018). One advantage of hadronic transport models is that the diffusion from the GC to the bubbles' edges can proceed with no significant energy losses, which is consistent with a long life for the FB of the order of ∼Gyr (Crocker & Aharonian 2011; Ackermann et al. 2014; Fang et al. 2017). Pure-hadronic scenarios, however, fail to reproduce the microwave haze observations: The synchrotron component produced by the secondary e^+e^- population would be too soft and three to four times lower than the observed emission. In order to reproduce WMAP data, it is necessary to invoke a primary source of CRe or reacceleration mechanisms for the secondary population.

Leptonic processes involve CRe interacting with the low-energy photons of the interstellar radiation field (ISRF). In this scenario, the GeV gamma-ray emission could be entirely attributed to IC scattering, and the lower-energy part of the CRe population can also naturally explain (fine-tuning the assumed average magnetic field within the FB) the microwave haze emission via synchrotron emission. The bremsstrahlung component from the CRe is negligible due to the low gas density in the region of the FB (in the literature, it is often quoted as $n_{\rm H} = 0.01$ cm^{-3}). Apart from reproducing the haze observations, leptonic scenarios also have the advantage that they easily explain the high-energy cutoff observed by the LAT: very-high-energy CRe (above tens of TeV) cool much more efficiently via IC and synchrotron energy losses (Yang & Ruszkowski 2017). However, pure-leptonic models set a stringent limit on the age of the FB because a CRe of TeV energies radiating due to both the Galactic magnetic field (via synchrotron) and the ISRF (via IC) exhausts its energy in a few hundred thousand years. This limits the age of the FB to be relatively young. Particles would need to be promptly accelerated and transported to the edges of the FB by extremely fast winds (like the jets observed in active galactic nuclei) unless reacceleration processes at recent times are invoked (see, e.g., Mertsch & Sarkar 2011; Cheng et al. 2014). It has been pointed out that the fast cooling of CRe is difficult to rectify with the observed uniformity of the GeV emission throughout the FB: given the ISRF gradient with Galactic latitude, the energy density of the CRe would need to compensate for that in order to match the observed uniform brightness (Yang & Ruszkowski 2017).

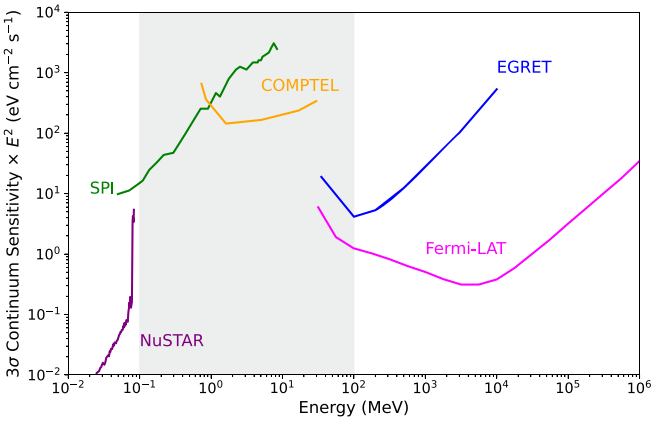

Figure 1. Sensitivities of past and present instruments operating around and within the MeV gap (gray shaded region).

Hybrid models, where populations of CRe and CRp coexist within the FB, can also be used to explain the observations throughout the electromagnetic spectrum of the FB (Fang et al. 2017). A two-zone hybrid model, with CRe populating the lower part of the bubbles and CRp inhabiting the cocoons, is also appealing and worth considering for future investigations.

In summary, as of now, both leptonic and hadronic scenarios can explain the observed GeV emission observed by the LAT, with different strengths and weaknesses for the two cases. HAWC's high-energy gamma-ray upper limits are not stringent enough to rule out a hadronic component, and high-energy neutrino observatories are not sensitive enough (and will not be soon; Fang et al. 2017) to unambiguously detect neutrinos from the FB, which would confirm a hadronic emission scenario.

If we look at currently operating high-energy telescopes from X-rays to very-high-energy gamma rays, we would notice a "gap" in sensitivity between ∼100 keV and ∼100 MeV, with the worst performance around 1–10 MeV. We illustrate the gap in sensitivity in the MeV band in Figure 1. This poorly explored band of the electromagnetic spectrum is called the MeV gap. The number and variety of possibilities that

[12] The eRB average X-ray surface brightness between 0.6 and 1 keV, as quoted in Predehl et al. (2020), is $(24) \times 10^{-15}$ erg cm^{-2} s^{-1} arcmin^{-2}, the two numbers in the range corresponding to the northern and the southern FB, respectively.

[13] https://icecube.wisc.edu

[14] https://antares.in2p3.fr

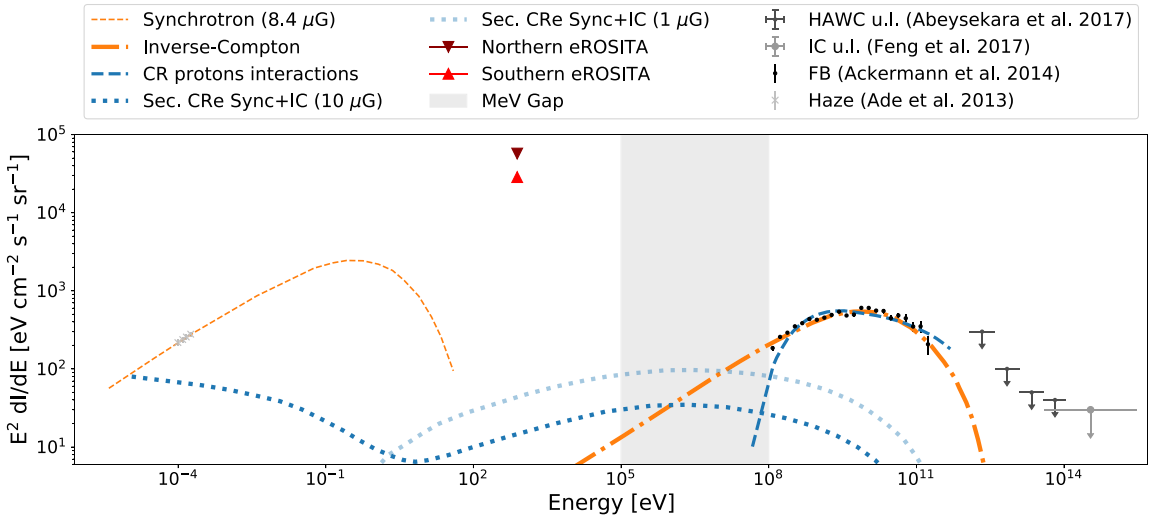

Figure 2. Compilation of spectral measurements of the FB together with models for the emission components. The orange lines show the IC and synchrotron emission from the same benchmark population of electrons (Ackermann et al. 2014) obtained from the best-fit to FB Fermi-LAT measurements (black points) and Planck microwave haze measurement (Planck Collaboration 2013) (silver crosses). The blue lines show primary and secondary gamma-ray emission from hadronic processes. Also shown are the HAWC and IceCube upper limits for very-high-energy gamma rays and neutrinos, respectively, and the average surface brightness of the eRBs (red points). The shaded gray region marks the MeV gap.

observations in the MeV gap can open for the astrophysical community are simply extraordinary (see, e.g., Andritschke et al. 2006; De Angelis et al. 2018; McEnery et al. 2019), from the study of nuclear lines from supernovae, to the diffuse 511 keV emission possibly related to dark matter, to a whole class of Galactic and extragalactic astrophysical sources shining bright in this energy range. In particular, in this paper, we discuss the advantages that MeV observations of the FB would provide for unveiling the underlying emission mechanisms. In Figure 2 we highlight how within the MeV energy band the gamma-ray emission expected from the leptonic and the hadronic scenarios show remarkably different behaviors, which could be captured by a MeV telescope sensitive enough to detect large-scale emission from the FB.

The paper is structured as follows. In Section 2 we discuss the detection and imaging principles for MeV gamma-ray observations, and we provide some examples of past, future, and proposed MeV mission designs. In Section 3 we present a procedure to compute the sensitivity of MeV telescopes to MeV emission from the FB and illustrate the case for past, future, and potential future Compton and Compton-pair telescopes. The last section, Section 4, is devoted to the summary and the conclusions, and we include two appendices with details about the hadronic and leptonic models used in this work and the scaling of the sensitivity in the Compton regime with the extension of a source.

2. Measuring MeV Gamma Rays

For the most part, the universe is transparent to hard X-rays and gamma rays below tens of GeV, which ironically also makes photons in this energy range challenging to detect. High-energy photons interact with matter in three different ways: below some tens to hundreds of keV (depending on the material), the dominant interaction mechanism is the photoelectric effect; at intermediate energies (tens of keV to tens of MeV), Compton scattering on quasi-free electrons has the highest cross section; and above some tens of MeV, e^+e^- pair production in the electric field of the ambient nuclei dominates.

2.1. MeV Gamma-Ray Detection Principles

In the MeV band the photoelectric effect is subdominant, and hence we focus here on the Compton and pair-production regimes.

In the pair-production regime, the secondary e^+e^- are typically energetic enough to propagate over macroscopic distances in the detector, leaving ionization tracks. For sufficiently high primary photon energies, the secondary particles may emit additional gamma rays interacting with the electric fields of ambient nuclei (Bremsstrahlung radiation), initiating a cascade or shower of electrons, positrons, and gamma rays. In the Compton regime, the scattered photon is emitted at a characteristic angle ϕ with respect to the primary photon direction and may undergo further Compton scattering processes before depositing the rest of its energy via the photoelectric effect. Depending on the energy transferred to the secondary electron, this particle may also travel over macroscopic distances and leave an ionization trail. In the following sections, Compton events for which the direction of the scattered electron is measured are referred to as "tracked Compton events" (TC events), and those without an electron track are called "untracked Compton events" (UC events).

While the interaction cross sections depend on the detector material, generally the cross sections for Compton scattering and pair production are several orders of magnitude lower than those for the photoelectric effect. MeV gamma-ray detectors thus require a large enough mass and volume to have a reasonable chance that gamma rays will interact in the detector and not just pass through.

2.2. Imaging MeV Gamma Rays

For instruments designed to observe gamma-ray bursts, imaging capabilities are often unnecessary. For the duration of the burst, the gamma-ray signal outshines the background, and

it is possible to provide a crude localization of the burst by comparing, e.g., the arrival times or count rates in different parts of the detector. However, imaging capabilities can be crucial for the performance of missions designed to study gamma-ray emission on longer timescales, allowing them to suppress the background, disentangle emission from multiple sources in the field of view (FoV), and study the morphology/substructure and extent of some gamma-ray sources.

There is no known mechanism to focus MeV gamma rays with a technology sufficiently tested for space missions.[15] "Imaging" is achieved by reconstructing the arrival directions of each incoming gamma-ray photon (on an event-by-event basis). This can only be achieved for Compton scattering and pair-production events.

For Compton events, it is typically possible to measure the direction of the scattered photon (from the location of the first and second interactions in the detector) and the Compton angle ϕ (from the deposited energies). The arrival direction of the primary photon projected back on the sky is then constrained to lie on a circle with an opening angle of 2ϕ around the direction of the scattered photon. For imaging instruments, the angular resolution (uncertainty in the width of the Compton ring) is typically dominated by the uncertainty in ϕ, which is determined by the energy resolution. The FWHM of the distribution of the difference between the true and reconstructed Compton angle is often referred to as the ARM (angular resolution measure).

Unambiguously measuring the arrival direction of the primary photon is not possible given just the scattered photon and Compton angle. Statistical methods exist to extract the number and likely location(s) of gamma-ray sources in the FoV, even in the presence of diffuse background, as long as a sufficient number of photons are observed from each source.

TC events have a second constraint on the arrival direction of the primary photon, given by the "scatter plane": the primary gamma-ray direction must be coplanar with the directions of the Compton electron and the scattered photon. The uncertainty in the scatter plane is called the "scatter plane deviation" (SPD). Due to uncertainty in the SPD, it generally reduces the Compton circle to an arc segment rather than a point. The scatter plane constraint helps reduce ambiguities and distinguish weak sources from the chance overlap of Compton circles.

The angular resolution of a Compton telescope can be improved to as fine as a fraction of a degree by means of coded aperture masks (Forot et al. 2007; Galloway et al. 2018). However, the introduction of a coded aperture mask may also result in a reduction of the instrumental FoV and of the efficiency (fewer photons interacting in the detector), and potentially in an increased instrumental background due to activation of the mask materials. Furthermore, coded masks suppress diffuse emission on spatial scales larger than the typical solid angle covered by the mask pixels: this results in an improved sensitivity to point sources, but it is detrimental for detecting large-scale diffuse emission.

In the case of gamma rays interacting via e^+e^- pair production (which we will call "P events"), the direction of the primary photon can be estimated from a combination of the tracks of the electron and the positron. The angular resolution is described by the point-spread function (PSF), the distribution of reconstructed arrival directions for gamma rays from a point source at a large distance. The PSF is typically radially symmetric around the true direction, with a Gaussian peak but larger tails (e.g., the PSF of the Fermi-LAT (Atwood et al. 2009) is well described by a King function; Read et al. 2011). The width of the distribution depends on the instrument and on the energy of the incoming photon.

2.3. Some Examples of MeV Gamma-Ray Telescopes

The Imaging Compton Telescope COMPTEL (Schoenfelder et al. 1993) was one of four instruments on board NASA's Compton Gamma-Ray Observatory (CGRO)[16] devoted to the exploration of the gamma-ray sky. CGRO operated from 1991 to 2000, orbiting Earth at an altitude of ∼450 km with a 28°.46 orbital inclination. The COMPTEL telescope detected gamma rays with energies between 0.8 and 30 MeV via Compton interactions of the photons with two layers of scintillators. The energy resolution was 10%–5% (at 1 and 20 MeV, respectively). COMPTEL had an FoV of ∼1.5 sr and covered the entire sky in 340 pointings with roughly 2 weeks' exposure each. The exposure was not uniform across the sky as shown in Figure 2 of Strong & Collmar (2019).

Also on board CGRO, the Energetic Gamma Ray Experiment Telescope (EGRET) (Hartman et al. 1992) employed spark chambers for detected gamma rays between 20 MeV and 30 GeV that converted into a e^+e^- pair within the instrument. The energy resolution was about 20% over the central part of the energy range; EGRET's effective area was about 1500 cm^2 between 200 MeV and 1 GeV, falling rapidly at higher and lower energies and with an approximately off-axis Gaussian profile with FWHM of ∼40°. EGRET has been succeeded by the Fermi-LAT above 100 MeV (Atwood et al. 2009).

The Compton Spectrometer and Imager (COSI) (Tomsick et al. 2019; Zoglauer et al. 2021) is a Compton telescope that will survey the sky between 0.2 and 5 MeV with a wide FoV (⩾25% of the sky). The instrument is designed and optimized to detect spectral lines such as the 511 keV line from positron annihilation and gamma-ray spectral lines from radioactive decays of isotopes produced by stellar nucleosynthesis, crucial probes of the evolution of massive stars and their supernova explosions. COSI will also measure polarization in the same energy range, which will provide unique new insights into the underlying physics of astrophysical jets and other particle acceleration regions. In 2021 October, COSI was selected by NASA to continue development as a Small Explorer mission, to be launched within the next 5 yr. COSI will be key to accomplishing the great science enabled by the observations in the MeV energy band.[17] Before being developed as a space-based mission, COSI's technology was tested in several balloon campaigns (see Table 1), which resulted in more than one month of data taking. COSI's selection as a future space-based explorer mission is of interest to the wide community of nuclear physicists and medium-gamma-ray astrophysicists.

Other proposed space-based missions to operate in the MeV gap include eASTROGAM (De Angelis et al. 2017) and

[15] Multilayer Laue lenses (Murray et al. 2019). Tungsten/silicon carbide multilayers with reduced interface roughness can focus X-rays above 100 keV and up to 250 keV (Windt et al. 2003; Jensen et al. 2005). However, this technology has not been tested in space-based applications.

[16] https://heasarc.gsfc.nasa.gov/docs/cgro/cgro.html

[17] For more about the science enabled by MeV astrophysical observations we suggest the many white papers on the topic (e.g., Zoglauer 2006; De Angelis et al. 2018).

Table 1
Summary of Some Characteristics of Previous, Current, Future, and Proposed Imaging Compton and Compton-pair Telescopes in the MeV Band

Instrument	Detector Type	Energy (MeV)	FoV (sr)	Obs. Mode	Mission Size	Mission Status
COMPTEL	Compton	0.8–30	1.5	Pointed	Great Obs. (CGRO)	Ended
EGRET	Pair	20–30000	0.4	Pointed	Great Obs. (CGRO)	Ended
Fermi-LAT	Pair	$20-{>}3\times10^5$	>2	Survey	Space probe[a]	Surveying
COSI balloon	Compton	0.2–5	3.1	Survey	Balloon-borne	Campaigns[b]
COSI	Compton	0.2–5	3.1	Survey	Space small	Launch in 2025
eASTROGAM	Compton-pair	0.3–3	>2.5	Survey	Space medium	Concept
AMEGO	Compton-pair	0.2–10000	>2.5	Survey	Space probe	Concept
AMEGO-X	Compton-pair	0.3–1000	>2.5	Survey	Space medium	Concept
GECCO	Compton	0.05/0.1–∼10	∼1	Pointed	Space medium	Concept

Notes.
[a] This classification is based on the modern nomenclature for the cost metrics of NASA's space missions, which has been defined after Fermi selection.
[b] COSI 2016 (Wanaka, New Zealand), COSI 2014 (McMurdo Station, Antarctica).

AMEGO (Kierans & the AMEGO team 2020), which are examples of survey Compton-pair telescopes capable of measuring nuclear lines, continuum emission, and polarization; the All-sky Medium Energy Gamma-ray Observatory eXplorer (AMEGO-X) (Fleischhack 2021) is another example of an all-sky survey Compton-pair telescope with a smaller volume than the previous two, optimized for continuum measurements and focused on the observation of multimessenger sources, such as gamma-ray bursts for joint detection of gravitational waves and Galactic and extragalactic sources of high-energy cosmic rays and high-energy neutrinos;[18] GECCO (Moiseev 2021) is a pointing Compton telescope optimized to observe the GC and Galactic plane with the possibility of applying a coded aperture mask to greatly enhance its angular resolution and multiple-source discrimination power.

In Table 1 we summarize some of the key characteristics of the missions and mission concepts mentioned above.

3. Source Sensitivity of MeV Telescopes

3.1. Background Estimation

For the prediction of the detection sensitivity of an instrument to a given source, a crucial element is a realistic estimate or a measurement of the background. As an example, we show the background flux measured by COMPTEL in Figure 3, in comparison to the mid-latitude-Galactic and extragalactic background components, for which we provide more details in the next paragraph. The COMPTEL background flux was derived from the in-flight background counts reported in Table 12 of Schoenfelder et al. (1993): note that these background counts correspond to the specific event selection declared in Section 8.1 of Schoenfelder et al. (1993). We derive the flux by dividing the counts by the effective exposure reported in Table 13 of that reference for the same energy bins and scaled for the radius of a 1 sr region (see Appendix B). The measured COMPTEL background is up to a factor of 35 greater than the total astrophysical gamma-ray intensity: it is evident how the instrumental background is an important consideration for Compton telescopes, and in the case of COMPTEL it is the dominant source of background.

A guaranteed astrophysical background from the FB region is represented by the diffuse astrophysical background, which has two components: the extragalactic gamma-ray background

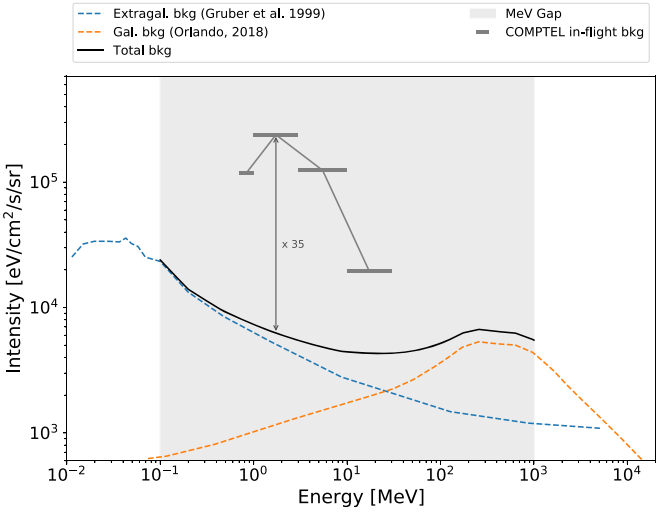

Figure 3. Galactic (dashed light blue line) and extragalactic (dashed orange line) astrophysical background components, and the sum of the two (solid black line). The gray solid line illustrates the in-flight-measured background by COMPTEL as reported in Schoenfelder et al. (1993) scaled for a region of 1 sr extension (see text for details).

and the Galactic diffuse emission. We are assuming that the contribution from point sources within the FB region is known, sufficiently well modeled, and subtracted (and/or masked away following the technique used, in the pair-production regime, by Ackermann et al. 2014). Once the instruments are in orbit, we expect that they will detect and characterize the point-like sources, which will allow this approach to be used. We note, however, that any mismodeling of the detected sources would contaminate the FB measurement. The extragalactic background can be assumed to be isotropic, and we consider, for our simulations, the measured spectrum of diffuse cosmic hard X-rays by High Energy Astronomical Observatory 1 (Gruber et al. 1999). The Galactic diffuse emission is not isotropic, depending strongly on Galactic latitude, especially below $|b|<10°$. Here, we consider the spectrum of the total Galactic diffuse emission at intermediate latitudes ($10°<|b|<20°$) estimated by Orlando (2017), and for simplicity, we consider it to be isotropic within the FB region. This assumption is a conservative choice to estimate the sensitivity to detect the FB: the measured total diffuse emission is less bright at higher latitudes, which would result in better sensitivity. However, an accurate model of the Galactic diffuse emission morphology is

[18] AMEGO-X will be proposed in the next NASA call for medium-size missions.

expected to be achievable for the actual measurement of the MeV FB emission with flight data, with contributions from components whose intensities are currently uncertain, such as gamma-ray emission associated with the Loop I and Loop IV radio filaments, which are well determined by the data. With these considerations, systematic uncertainties of the model for the non-FB Galactic interstellar emission will not be a limiting factor for the sensitivity of the measurement.

Figure 3 (left) shows the astrophysical diffuse emission discussed above. On top of the astrophysical background, MeV gamma-ray detectors typically suffer from large instrumental backgrounds, which dominate the trigger rates on timescales longer than a few minutes. Such backgrounds include contributions from gamma rays emitted by Earth's atmosphere, charged particles (cosmic rays) passing through the detector, and radioactive decays from activation induced by the latter. The charged-particle background can be reduced by surrounding the instrument with plastic scintillator plates or similar sensors that can detect and veto the passage of charged particles. The activation background, which is mostly irreducible, is composed of radioactive decays within the instrument due to activation of the detector material caused by cosmic-ray interactions (dominant in the UC and TC regimes) and secondary gamma rays produced by the impact of cosmic rays in the outer layers of the spacecraft (e.g., the micrometeoroid shielding), before the vetoing scintillators. The irreducible instrumental backgrounds strongly depend on the spacecraft design, materials, and orbital altitude and inclination and need to be carefully evaluated through detailed simulations and in-flight measurements.

3.2. Prescription to Derive MeV Telescope Sensitivity to the FB

We define the FB region as a circular region with a radius $R_{\rm FB} = 20^\circ$ covering the intermediate latitudes with centers at $l = 0$ and $b = \pm 30^\circ$. The 3σ sensitivity in a given energy bin is obtained by estimating the total number of counts needed to have a signal-to-noise ratio $\mathrm{S/N} = 3$ given the total number of background events expected while observing the FB region:

$$\mathrm{S/N} = \frac{N_{\rm sig}^{\Delta E}}{\sqrt{N_{\rm sig}^{\Delta E} + N_{\rm bkg}^{\Delta E}}}. \quad (1)$$

In the P-event regime, besides running simulations, it is possible to estimate the background counts from the expected background flux in photons per unit area, time, and solid angle in the energy bin of interest, $I_{\rm bkg}^{\Delta E}$, and correcting by the effective area and the observation time of the telescope:

$$N_{\rm bkg}^{\Delta E} = t_{\rm obs}\, I_{\rm bkg}^{\Delta E}\, A_{{\rm eff},\bar{\Theta}}^{\bar{\Delta E}}\, \Omega, \quad (2)$$

where $A_{\rm eff}^{\bar{\Delta E}}(\theta)$ is the average effective area of the telescope in the energy range considered and off-axis angle range Θ within the FoV, and with Ω being the solid angle of the FB region ($\Omega = 2\pi(1 - \cos(R)) \sim 0.38$ sr). The observation time for wide-FoV survey-like telescopes can be estimated as $t_{\rm obs} = t_{\rm mission}\frac{\rm FoV}{4\pi} f$, where f is a factor that takes into account possible dead times due to Earth occultation or temporal survey suspensions (e.g., due to targeted pointing or south Atlantic anomaly crossing). For a pointing instrument, one can assume to point to the center of one of the FB at a time and take into account the dependence of the effective area on the off-axis angle (the angle between the boresight of the instrument and a position in the sky) within the FB region with the following substitution:

$$A_{{\rm eff},\bar{\Theta}}^{\bar{\Delta E}}\,\Omega \;\rightarrow\; 2\pi \int_0^{20^\circ} A_{\rm eff}^{\Delta E}(\Theta)\sin(\Theta)\, d\Theta. \quad (3)$$

The number of signal counts, $N_{\rm sig}$, needed to achieve a 3σ detection given $N_{\rm bkg}$ can be obtained by requiring $\mathrm{S/N} = 3$ in Equation (1), and the flux sensitivity for P events can be obtained as

$$F_{\mathrm{S/N}=3}^{\Delta E} = \frac{N_{\rm sig}^{\Delta E}}{t_{\rm obs}\, A_{{\rm eff},\bar{\Theta}}^{\bar{\Delta E}}}\ [\mathrm{cm^{-2}\ s^{-1}}]. \quad (4)$$

For UC events, if the point-source sensitivity is known, it is possible to determine the sensitivity for the FB region by means of the scaling of the sensitivity with the square root of the background event count (for the case of a background-dominated source), or equivalently with the power of one-quarter of the extended source area (see Appendix B):

$$F_{\mathrm{S/N}=3}^{\Delta E} = F_{\mathrm{S/N}=3}^{\mathrm{PS},\Delta E}\left(\frac{\Omega}{\pi R_{\mathrm{ARM}/2}^2}\right)^{1/4}, \quad (5)$$

where $R_{\mathrm{ARM}/2}$ is half-width at half-maximum (HWHM) of the ARM distribution in steradians for the energy bin considered. Note that the angular extension Ω in Equation (5) is limited by the angular resolution of the instrument.

For TC events, the scaling in sensitivity with the extension of the source should be somewhere in between the softer scaling for UT events and the stronger scaling for P events. Estimating such scaling is beyond the purpose of this paper. Hence, in this work, unless stated otherwise, we treat TC events as P events adopting Equation (2) to estimate the sensitivities, namely, we are assuming the worst-case scenario in which TC sensitivities scale as P sensitivities with the extension of the source.[19]

The sensitivity to the pair of bubbles, assuming that they have identical emissions, is obtained by combining the sensitivity to one bubble as $I_{\rm 2FB} = \frac{1}{\sqrt{2}} I_{\rm 1FB}$.

3.3. COMPTEL, COSI, and AMEGO-X Mission Concept Sensitivities

COMPTEL was designed to operate in the UC regime, so we followed the procedure for the UC regime described in the previous section to scale the point-source continuum sensitivity of COMPTEL to a 1 sr extended region. We use the point-source continuum sensitivity reported in Table 13 of Schoenfelder et al. (1993) and the 1σ ARM width illustrated in Figure 28 of the same paper. Such sensitivity is for a 2 week exposure; hence, knowing that the sensitivity scales as the squared root of the time, we obtain the sensitivity for the average exposure within the FB region as reported in Strong & Collmar 2019: the average exposure in the FB region for the whole mission is about 55

[19] Equation (2) still holds for TC events in the case where it is possible to select events (which look like arcs in the sky) coming from the region of interest without losing too much effective area. This selection can be done, for example, by discarding all events whose arc is not fully contained in the region of interest, or, more loosely, keeping all events whose arc falls within the region for more than, say, 95% of its extension. Intuitively, this is the case in which the extension of the arc for the majority of the events does not exceed the size of the FB region.

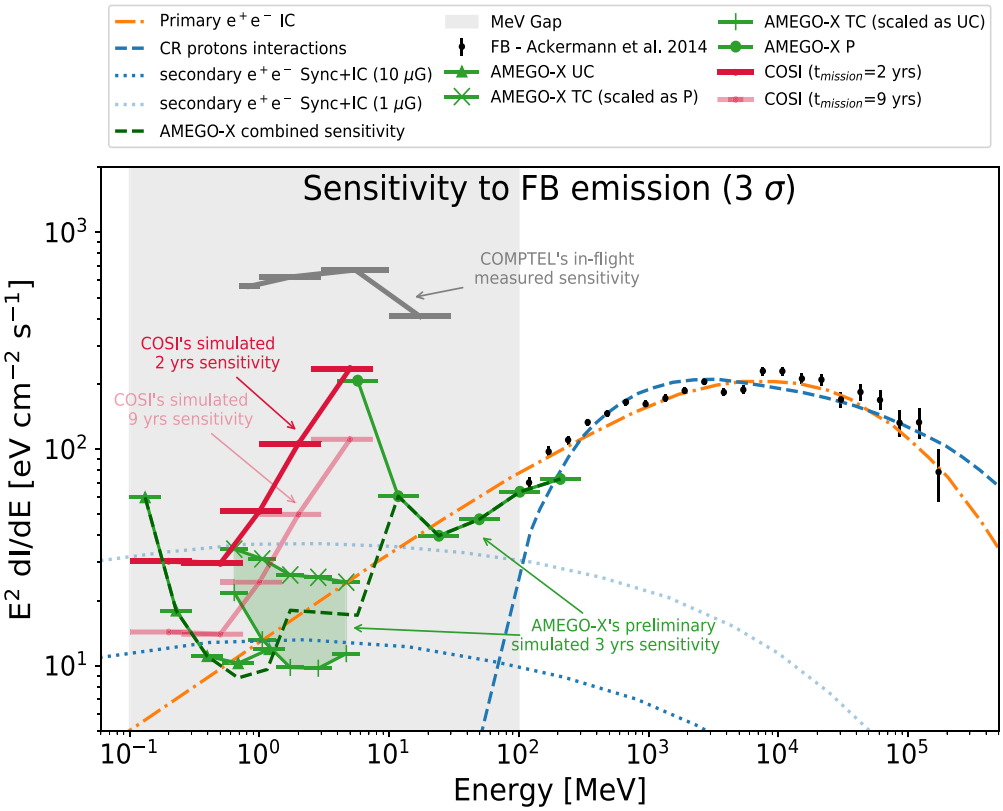

Figure 4. Combined FB sensitivity for both bubbles in the MeV gap for COSI, COMPTEL, and AMEGO-X. COMPTEL sensitivity is derived from Table 13 of Schoenfelder et al. (1993) and scaled for the FB extension as detailed in the text. COSI sensitivity has been provided by the COSI team and is based on Geant4 (Allison et al. 2016) simulations using the COSI design requirement performance for a disk-like source with a 20° radius. AMEGO-X sensitivity for UC events has been obtained by scaling the point-source sensitivity as detailed in the text; the two sensitivity curves in the TC regime have been derived by treating TC events as UC ones (green "+") or as P events (green "x"). Both are based on preliminary background simulations run with an ARM cut of 20° simulations. The combined AMEGO-X sensitivity is reported (dark-green dashed line), where for UC events we considered the median of the sensitivity curves obtained by treating TC events as UC and P events. The orange line shows the IC emission that best fits the LAT-measured FB spectrum in Ackermann et al. (2014). The blue lines show primary and secondary gamma-ray emission from hadronic processes. The shaded gray region marks the MeV gap.

days. In Figure 4 we show that the sensitivity of COMPTEL is simply insufficient to detect the FB.

COSI's sensitivity curves are illustrated in Figure 4.[20] We report the 3σ sensitivity curves for the nominal 2 yr of the mission (red curve) and for 9 yr (light red curve). During its nominal lifetime of 2 yr, COSI would observe the FB region for approximately 6 months and detect a hadronic component from the FB (for magnetic field values $\lesssim 1\,\mu$G). Interesting upper limits could be set below ~ 1 MeV, extending the mission beyond the nominal lifetime.

We also report the case of the AMEGO-X Compton-pair telescope concept in Figure 4. The UC, TC, and P-event regimes are shown in green and have been obtained following the procedure described in Section 3. In particular, the sensitivity for the UC regime has been derived using Equation (5) from the point-source continuum sensitivity estimated through simulations.[21] The sensitivities are based on simulations of the expected background rates and gamma-ray effective area of AMEGO-X, using a preliminary detector model. The background simulations, similarly to the ones used for COSI, include contributions from cosmic rays (protons, alpha particles, and electrons), instrument activation, atmospheric background, and the extragalactic (isotropic) gamma-ray background. More refined simulations will only become available when the instrument design is finalized. Should the mission proceed, the background rates will be derived from actual in-flight measurements for which an accuracy well under 10% is expected. AMEGO-X is designed to operate in survey mode, with a wide FoV of 2.5 sr in the P regime and up to 3.6 sr in the Compton regime. Figure 4 shows that an instrument like AMEGO-X would be able to detect a pure-leptonic emission from the FB almost in the entire energy range of the MeV gap in a 3 yr sky survey,[22] and it could detect hadronic (secondary leptonic) emission in an energy range that depends on the magnetic field present within the FB. In the case of hybrid scenarios, the detection of a spectral break in the MeV energy range would constrain the relative contribution of the leptonic component over the hadronic one populating the FB, and, once the primary hadronic population is fixed, the intensity of the secondary leptonic emission would constrain the magnetic field within the bubbles.

The sensitivity estimations presented in this section come with some caveats. First, the uniformity of the FB is an approximation, and some level of nonuniformity in the intensity distribution and spectrum might affect the sensitivity

[20] COSI sensitivity curves have been made available through private communication with John Tomsick, PI of the COSI mission.

[21] AMEGO-X point-source sensitivities have been carried out by the AMEGO-X team with MEGALib (Zoglauer et al. 2006). For the TC and P regimes, we used Equation (4) to derive the sensitivities, where preliminary background simulations and simulated instrument effective area have been provided by the AMEGO-X team (https://asd.gsfc.nasa.gov/amego-x/).

[22] Three years is the nominal duration for NASA's Medium Explorer missions.

estimates (e.g., and increase the S/N in the brighter regions). Second, as already mentioned, the estimation of the background components is based on simulations (except for the case of COMPTEL). Once an instrument is in orbit, the instrumental background can be calibrated, and measurements of the actual astrophysical background and sources can be obtained within a certain level of accuracy (expected to be of the order of a few percent or lower, based on similar, previously developed instruments). For example, the internal activation background can be modeled based on the strength of detected nuclear lines, shields around the instrument reject the charge particle background, and the upward-moving atmospheric background photons can be characterized by occasionally pointing the instrument at the atmosphere. In addition, COSI and AMEGO-X will have several additional particle and background detectors on board to monitor the space radiation environment and enable their accurate characterization. As a consequence, we expect to be able to characterize the background with an uncertainty significantly below 10% (the exact number depends on many factors and will only be known after launch). Finally, our computation of the AMEGO-X sensitivity does not include any event-quality cut, which would reduce the background contamination and, hence, increase the S/N. In Appendix C, as an example, we show how the AMEGO-X FB sensitivity changes when scaling the background rate, and we present a simple procedure for estimating the variation of the sensitivity by admitting a certain level of uncertainty on the simulations.

4. Conclusions

In this work, we showed the potential for observations of MeV gamma rays to solve the long-standing mystery behind the origin of the FB emission, which is a crucial aspect in understanding how these apparently giant structures themselves originated.

First, we noted how pure-leptonic and pure-hadronic emission scenarios diverge in the MeV gap. Hence we discussed the main characteristics of some instruments operating in this energy range. In particular, we computed the sensitivity of some past and future MeV telescopes. We showed that COMPTEL was not sensitive enough to detect the predicted emission from the FB, while COSI, recently selected by NASA's Small Explorer missions program, could detect a hadronic component at 0.1−0.6 MeV already within its prime mission time (2 yr) or could set upper limits on the FB emission in this energy range, constraining the magnetic field strength within the bubbles for hadronic scenarios. Additionally, we illustrate the concept of AMEGO-X as an example of a future wide-FoV survey Compton-pair telescope: according to preliminary simulations, AMEGO-X would be sensitive to a pure-leptonic component from the FB over almost the entire energy range of the MeV gap (100 keV–100 MeV), after three years of survey.

Additionally, we noted how, in the case of a hybrid scenario, in which both a leptonic and a hadronic component exist in the emission of the FB, the observation of a spectral break in the MeV band would constrain the relative contribution of the two populations. Additionally, the intensity of the secondary leptons generated in hadronic interactions would constrain the magnetic field within the FB. This scenario would be accessible to a wide-FoV survey Compton-pair telescope sensitive to the FB emission throughout almost the entire MeV gap energy range.

In conclusion, MeV gamma-ray observations will be able to resolve the emission mechanisms and origin of the Fermi Bubbles. The future Compton telescope COSI, on top of the primary science it was designed for, will shed some light on the main emission mechanism from the FB. A Compton-pair survey telescope such as AMEGO-X has the potential to ultimately unveil the origin of the FB emission.

M.N. acknowledges John Tomsick and the COSI team for providing COSI's continuum sensitivities, and Eric Burns for the fruitful discussions and for encouraging writing this manuscript. We acknowledge Regina Caputo and the AMEGO-X team for the work done on the simulations and instrument performance. The material is based upon work supported by NASA under award number 80GSFC21M0002.

Appendix A
Pure-leptonic and Pure-hadronic Models

A careful morphological and spectral characterization of the FB was performed by the Fermi-LAT collaboration in Ackermann et al. (2014). In that work, pure-leptonic and pure-hadronic scenarios were evaluated to describe the average FB spectrum. We consider the best-fit models for the two scenarios proposed by Ackermann et al. (2014) and look at the expected gamma-ray emission in the MeV band.

In Ackermann et al. (2014), the spectrum of the cosmic-ray electron (CRe) population for the pure-leptonic model was assumed to be a power law with an exponential cutoff $\propto E^{-n}e^{E/E_{\rm cut}}$, where the best-fit parameters were found to be $n = 2.17 \pm 0.05$ and $E_{\rm cut} = 1.25 \pm 0.13$ TeV. This population of electrons and positrons interacts with the ISRF, which was modeled as in the GALPROP code (Strong et al. 2009). The resulting IC spectrum is reported in Figure 2 as a dotted–dashed orange line. The less-energetic side of the CRe population also interacts with the magnetic field present inside the bubbles and produces synchrotron emission; a magnetic field intensity of $B = 8.4 \pm 0.2\ \mu$G[23] has been found to reproduce the microwave haze quite well (see the dashed orange line in Figure 2).

As for the hadronic model adopted in Ackermann et al. (2014), the assumed CRp spectrum was a power law with exponential cutoff $\frac{dn(p)}{dp} \propto p^{-n}e^{pc/E_{\rm cut}}$, with best-fit values being $n = 2.13 \pm 0.01$ and $E_{\rm cut} = 14 \pm 7$ TeV, and assuming an ionized hydrogen column density of $n_{\rm H} = 0.01\ {\rm cm}^{-3}$. The primary hadronic gamma-ray emission due to π^0 decay is shown in Figure 2 as a blue wide-dashed line, while the gamma-ray emission from the population of secondary leptons produced through hadronic interactions is reported in dotted lines for different values of the assumed magnetic field (1 and 10 μG in light and dark blue, respectively). It is evident that the synchrotron emission from the secondary leptons is not enough to reproduce the microwave haze (further comments about this can be found in Section 7.2 of Ackermann et al. 2014).

Appendix B
Untracked Compton Events Scaling with Source Extension

In Section 2 we briefly described the typical procedure for imaging with Compton events by back-projecting onto the sky

[23] It is worth mentioning the systematic error associated with the best-fit magnetic field intensity as quoted by Ackermann et al. (2014): $B = 8.4 \pm 0.2[{\rm stat}]^{+11.2}_{-3.5}[{\rm syst}]\ \mu$G.

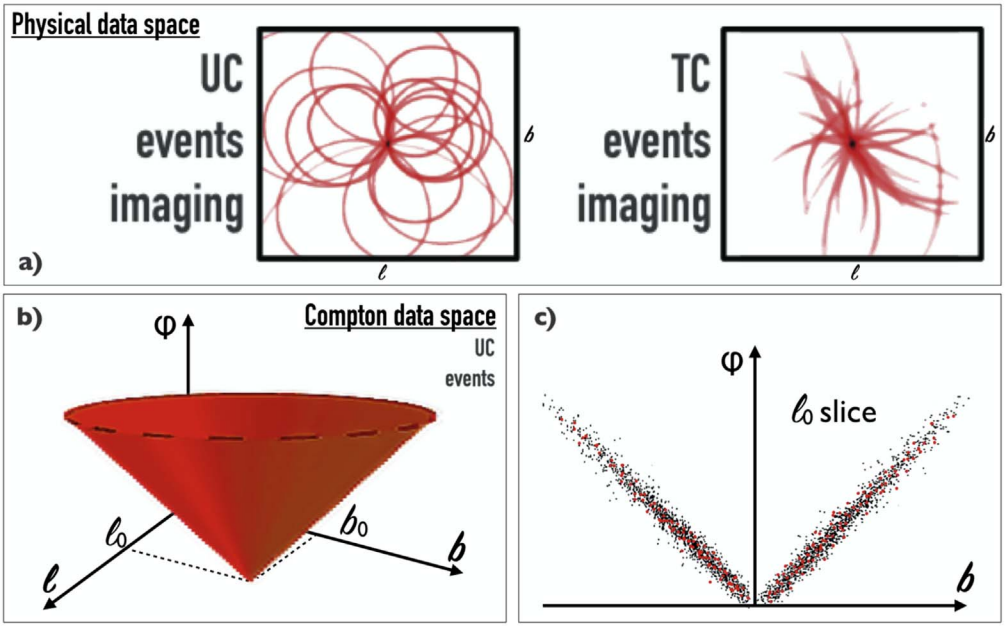

Figure 5. (a) Example of the imaging of a point source in Galactic coordinates in the untracked Compton (UC) regime and in the tracked Compton (TC) regime. (b) Events cone in Compton data space (ϕ, ℓ, b). (c) Median section of the Compton data space cone: the dispersion of the data points from the geometrical cone defines the width of the ARM distribution. The effect of the extension of a source on the Compton cone is to "thicken" the cone mantle by approximately the extension radius.

the Compton circles (UC regime) or event arcs (TC regime). A schematic illustration of the imaging of a point source for both the UC and TC regimes is given in Figure 5(a). It is clear, for UC events in particular, how the dominant background events can contaminate the image and wash out the signal from the source, and a selection based exclusively on the event circle locations in the 2D sky-coordinates space could result in a significant reduction of the effective area and worse sensitivities. So, when it comes to event selection and data analysis, a more convenient space to work with is the Compton data space (CDS), a 3D space whose coordinates are the direction of the axis of the event Compton circle (in sky coordinates) and the Compton scattering angle: each UC event is a point in this space. In the case of a perfect instrument (infinite energy resolution) and full absorption of the Compton-scattered photon in the second layer of the detector, the geometrical place defined by the events coming from a source in the sky (ℓ_0, b) is a cone with a 90° opening angle (Figure 5(b)). If the Compton-scattered photons are not fully absorbed and the instrument has a limited energy resolution, the events in the CDS are not perfectly on the cone but spread out from the surface of the cone, "thickening" the cone mantle: the distribution of the angular distance of the event points from the ideal cone is the ARM, whose FWHM gives the angular resolution of the instrument. Events from an extended source would result in a further thickening of the cone mantle to the size of the source radius extension. Assuming a disk-like extended emission and working in the Cartesian approximation of the cone, the number of background events that would be counted by selecting the events that fall in the cone mantle within a given ARM value is proportional to the volume:

$$N_{\rm bkg} \propto V_{\rm Cone\ mantle} = \frac{\pi}{3}h(h+R)^2 - \frac{\pi}{3}h(h-R)^2 = \frac{2}{3}\pi h^2 R, \tag{B1}$$

where h is the height (equal to the radius) of the cone in the CDS, and R is the half-thickness of the mantle (a.k.a. the extraction radius of the source). Recalling that the flux sensitivity (I_σ) scales with the square root of the background counts (in the background-dominated regime), we have

$$\frac{I_\sigma^{\rm ES}}{I_\sigma^{\rm PS}} \propto \frac{\sqrt{V_{\rm Cone\ mantle}^{\rm ES}}}{\sqrt{V_{\rm Cone\ mantle}^{\rm PS}}} = \sqrt{\frac{R^{\rm ES}}{R^{\rm PS}}} = \left(\frac{S^{\rm ES}}{S^{\rm PS}}\right)^{\frac{1}{4}}, \tag{B2}$$

where the labels PS and ES denote a point source and extended source respectively; $R^{\rm PS}$ is the HWHM of the ARM distribution, while $R^{\rm ES}$ is the radius of the disk that approximates the source extended emission; and $S^{\rm ES}$ is the area of the extended source (disk approximation), while $S^{\rm PS} \sim \pi {\rm ARM}_{\rm HWHM}^2$.

Appendix C
Sensitivity Scaling with the Background

In a background-dominated regime, such as the case considered in this study, the source sensitivity, given a fixed S/N, scales proportionally to the square root of the background counts. Using this relation, in Figure 6, we compare the AMEGO-X combined (UC+TC+P events) sensitivity with that obtained with a simulated background scaled by factors of 2 and 0.5. In the extreme case where the simulated background is enhanced by 100%, the AMEGO-X sensitivity would lie just above the predicted intensity of the leptonic model. Therefore, mismodeling the background intensity by anything less than 50% would not affect our conclusions.

Below 30 MeV, the background is dominated by the extragalactic astrophysical component plus the irreducible (what remains after well-defined quality cuts) instrumental component (cosmic rays, activation, and atmospheric gamma-ray photons). Once in orbit, we will be able to measure the rate and energy spectrum of the background very well using "off regions" with no gamma-ray source, as it is isotropic after Earth horizon cuts. To estimate how well we might be able to

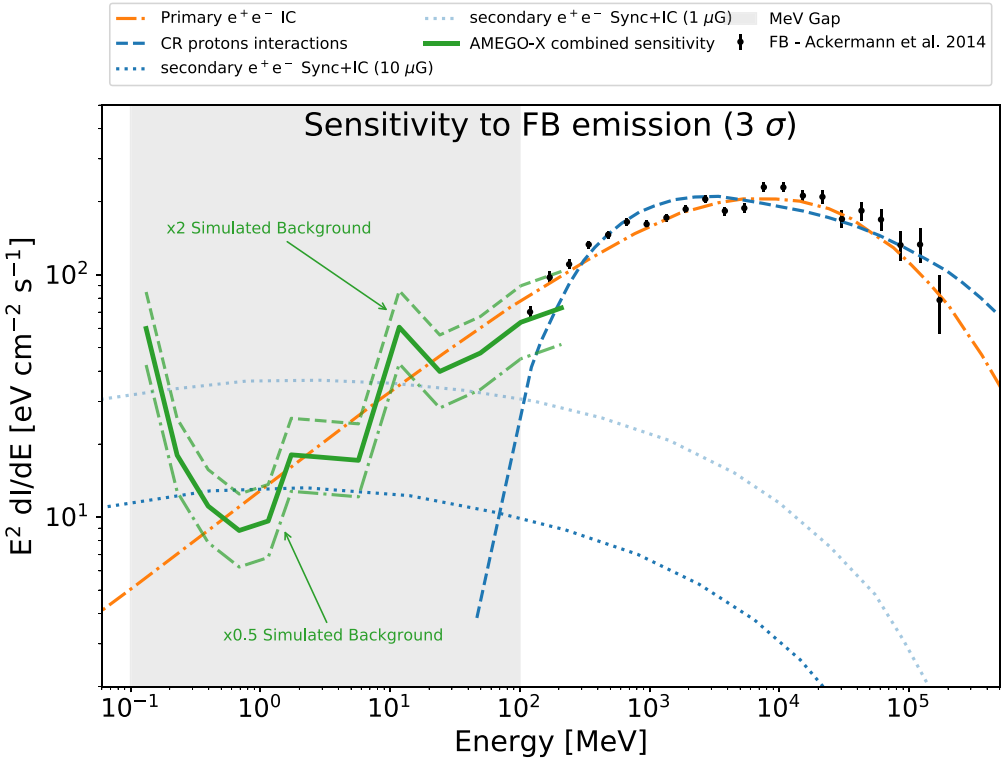

Figure 6. Variation of the AMEGO-X combined (3 yr) sensitivity if assuming a factor of 2 more and less background rate. The solid green line corresponds to the dashed dark-green line in Figure 4.

measure this background, we can look at other, similar gamma-ray instruments. Let us consider the Fermi-LAT isotropic background template. The flux uncertainty in the lowest bin provided (starting at 30 MeV) improved from 7% (pass 6 R3, after 1 yr in orbit) to 0.1% (pass 8 R3, after 8 yr in orbit).[24] Therefore, we believe that we will be able to measure the isotropic background for AMEGO-X with similar accuracy.

As mentioned in the main text, by applying some event-quality cuts, we will be able to enhance the S/N for the observation of the FB emission. Once such cuts are defined and applied, we would be able to determine the variation of the AMEGO-X sensitivity when admitting a given level of uncertainty on the background component. This estimation can be done by simply redefining Equation (1) as follows:

$$\mathrm{S/N} = \frac{N_{\mathrm{tot}}^{\Delta E} - \alpha N_{\mathrm{bkg}}^{\Delta E}}{\sqrt{N_{\mathrm{tot}}^{\Delta E}}} = \frac{N_{\mathrm{sig}}^{\Delta E} + (1-\alpha) N_{\mathrm{bkg}}^{\Delta E}}{\sqrt{N_{\mathrm{sig}}^{\Delta E} + N_{\mathrm{bkg}}^{\Delta E}}}, \qquad \text{(C1)}$$

where $\alpha = 1 \pm \mathrm{syst.}$ (where syst. stands for the systematic uncertainty).

ORCID iDs

Michela Negro https://orcid.org/0000-0002-6548-5622
Henrike Fleischhack https://orcid.org/0000-0002-0794-8780
Andreas Zoglauer https://orcid.org/0000-0001-9067-3150
Seth Digel https://orcid.org/0000-0002-5296-4720
Marco Ajello https://orcid.org/0000-0002-6584-1703

[24] Numbers from https://fermi.gsfc.nasa.gov/ssc/data/access/lat/BackgroundModels.html.

References

Abeysekara, A. U., Albert, A., Alfaro, R., et al. 2017, ApJ, 842, 85
Ackermann, M., Ajello, M., Albert, A., et al. 2017, ApJ, 840, 43
Ackermann, M., Albert, A., Atwood, W. B., et al. 2014, ApJ, 793, 64
Adrián-Martínez, S., Albert, A., Al Samarai, I., et al. 2014, EPJC, 74, 2701
Allison, J., Amako, K., Apostolakis, J., et al. 2016, NIMPA, 835, 186
Andritschke, R., Zoglauer, A., Kanbach, G., Bloser, P. F., & Schopper, F. 2006, in The Compton and Pair Creation Telescope MEGA, ed. P. von (Dordrecht: Springer), 395
Atwood, W. B., Abdo, A. A., Ackermann, M., et al. 2009, ApJ, 697, 1071
Cheng, K. S., Chernyshov, D. O., Dogiel, V. A., & Ko, C. M. 2014, ApJ, 790, 23
Crocker, R. M., & Aharonian, F. 2011, PhRvL, 106, 101102
De Angelis, A., Tatischeff, V., Grenier, I., et al. 2018, JHEAp, 19, 1
De Angelis, A., Tatischeff, V., Tavani, M., et al. 2017, ExA, 44, 25
Dobler, G. 2012, ApJL, 760, L8
Dobler, G., Finkbeiner, D. P., Cholis, I., Slatyer, T., & Weiner, N. 2010, ApJ, 717, 825
Fang, K., Su, M., Linden, T., & Murase, K. 2017, PhRvD, 96, 12
Fleischhack, H. 2021, 37th Int. Cosmic Ray Conf. (ICRC2021), 395, ed. A. Kappes & B. Keilhauer (Trieste: PoS), 649
Forot, M., Laurent, P., Lebrun, F., & Limousin, O. 2007, ApJ, 668, 1259
Galloway, M., Zoglauer, A., Boggs, S. E., & Amman, M. 2018, A&A, 614, A93
Gruber, D. E., Matteson, J. L., Peterson, L. E., & Jung, G. V. 1999, ApJ, 520, 124
Hartman, R. C., Bertsch, D. L., Fichtel, C. E., et al. 1992, NASCP, 3137, 116
Herold, L., & Malyshev, D. 2019, A&A, 625, A110
Hooper, D., & Slatyer, T. R. 2013, PDU, 2, 118
Jensen, C. P., Madsen, K. K., & Christensen, F. E. 2005, ExA, 20, 93
Kierans, C. A. & the AMEGO team 2020, Proc. SPIE, 11444, 1144431
McEnery, J., van der Horst, A., Dominguez, A., et al. 2019, BAAS, 51, 245
Merloni, A., Predehl, P., Becker, W., et al. 2012, arXiv:1209.3114
Mertsch, P., & Sarkar, S. 2011, PhRvL, 107, 091101
Moiseev, A. 2021, 37th Int. Cosmic Ray Conf. (ICRC2021), 395, ed. A. Kappes & B. Keilhauer (Trieste: PoS), 648
Moulin, E., Montanari, A., Malyshev, D., & Malyshev, D. 2021, 37th Int. Cosmic Ray Conf. (ICRC2021), 395, ed. A. Kappes & B. Keilhauer (Trieste: PoS), 791
Murray, K. T., Pedersen, A. F., Mohacsi, I., et al. 2019, OExpr, 27, 7120

Orlando, E. 2017, MNRAS, 475, 2724
Planck Collaboration 2013, A&A, 554, A139
Predehl, P., Sunyaev, R. A., Becker, W., et al. 2020, Natur, 588, 227
Razzaque, S., & Yang, L. 2018, Galax, 6, 47
Read, A. M., Rosen, S. R., Saxton, R. D., & Ramirez, J. 2011, A&A, 534, A34
Rubtsov, G., & Zhezher, Y. 2018, arXiv:1812.05228
Schoenfelder, V., Aarts, H., Bennett, K., et al. 1993, ApJS, 86, 657
Strong, A., & Collmar, W. 2019, MmSAI, 90, 297
Strong, A. W., Moskalenko, I. V., Porter, T. A., et al. 2009, arXiv:0907.0559
Su, M., & Finkbeiner, D. P. 2012, ApJ, 753, 61
Su, M., Slatyer, T. R., & Finkbeiner, D. P. 2010, ApJ, 724, 1044
Tomsick, J., Boggs, S. E., Zoglauer, A., et al. 2019, AAS Meeting, 223, 136.05
Vecchiotti, V., Pagliaroli, G., & Villante, F. L. 2021, arXiv:2107.03236
Windt, D. L., Donguy, S., Hailey, C. J., et al. 2003, ApOpt, 42, 2415
Yang, H.-Y. K., & Ruszkowski, M. 2017, ApJ, 850, 2
Zoglauer, A., Andritschke, R., & Schopper, F. 2006, NewAR, 50, 629
Zoglauer, A., Siegert, T., Lowell, A., et al. 2021, arXiv:2102.13158
Zoglauer, A. C. 2006, PhD thesis, TU München